

Photo- and Radioluminescence Properties of Eu^{3+} -doped Y_2O_3 Thick Film Phosphor Prepared via Chemical Vapor Deposition

Shogen Matsumoto, Taiga Watanabe, and Akihiko Ito*

Graduate School of Environment and Information Sciences, Yokohama National University,
79-7 Tokiwadai, Hodogaya-ku, Yokohama, Kanagawa, 240-8501, Japan

(Received October 17, 2021; accepted November 25, 2021; online published January 12, 2022)

Keywords: Y_2O_3 , CVD, thick film phosphor, photoluminescence, radioluminescence

We demonstrate the high-speed epitaxial growth of a Eu^{3+} -doped Y_2O_3 ($\text{Eu}^{3+}:\text{Y}_2\text{O}_3$) thick film phosphor grown on a (100) yttria-stabilized zirconia substrate by laser-assisted metal–organic CVD. The deposition rate was $42 \mu\text{m h}^{-1}$ and the resultant $7\text{-}\mu\text{m}$ -thick $\text{Eu}^{3+}:\text{Y}_2\text{O}_3$ film was optically transparent. Under UV and X-ray irradiation, the $\text{Eu}^{3+}:\text{Y}_2\text{O}_3$ thick film emitted red light originating from the ${}^5\text{D}_0 \rightarrow {}^7\text{F}_2$ transition of Eu^{3+} ions with a fluorescence decay time of 1.7 ms.

1. Introduction

Scintillators are phosphor materials with the ability to convert radiation such as X-rays, γ -rays, and α -particles into UV–visible photons.^(1–3) Scintillators coupled with photon detectors, such as photodiodes and CCD arrays, have been used as radiation imaging systems. Recently, radiation imaging systems have been used in such fields as nondestructive testing, nuclear medical imaging, and geological surveying.^(4–6) Scintillator screens with excellent luminescence and emission wavelengths compatible with photon detectors are required for radiation imaging. Tl^+ -doped CsI films and Tb^{3+} -doped $\text{Gd}_2\text{O}_2\text{S}$ (GOS) powder phosphors are used as scintillator screens because of their high luminescence yield and well-matched emission band (500–800 nm) with CCD detectors.^(7,8) Columnar and pixelated scintillators have been utilized to improve light yield and spatial resolution.^(9,10) Furthermore, thin scintillator screens of $10 \mu\text{m}$ or less can prevent light dispersion and are expected to be used in microtomography techniques.⁽¹¹⁾

Rare-earth sesquioxides have been intensively studied as laser gain media and scintillation phosphors because of their high optical transparency and isotropy and the wide range of possibilities of doping rare-earth activating centers. Y_2O_3 -based phosphors are promising materials for scintillation applications owing to their high density (5.01 g cm^{-3}) and wide band gap (6.1 eV).⁽¹²⁾ Eu^{3+} -doped Y_2O_3 ($\text{Eu}^{3+}:\text{Y}_2\text{O}_3$) has a high light yield ($32000 \text{ ph MeV}^{-1}$) with red emission (612 nm) that well matches CCD detectors.⁽¹³⁾ However, large Y_2O_3 single crystals cannot be easily grown because of the high melting point (2700 K) and the transition from the hexagonal to cubic phase at 2600 K.⁽¹⁴⁾ Although $\text{Eu}^{3+}:\text{Y}_2\text{O}_3$ thin films of up to 50 nm thickness

*Corresponding author: e-mail: ito-akihiko-xr@ynu.ac.jp
<https://doi.org/10.18494/SAM3698>

have been prepared by the sol–gel, chemical bath deposition, and CVD methods,^(15–17) they are too thin to stop radiation. From Henke's table, the mean free path of 8 keV X-rays in Y_2O_3 crystal has been calculated to be 7 μm .⁽¹⁸⁾ Fabricating such a thick film phosphor would typically be time-consuming using conventional deposition methods.

Laser-assisted metal–organic CVD is a rapid deposition process for functional thick films at a high deposition rate (10–300 $\mu\text{m h}^{-1}$).^(19–21) We previously reported transparent thick films of Eu^{3+} -doped Lu_2O_3 and $\text{Lu}_3\text{Al}_5\text{O}_{12}$ phosphors and $\text{Y}_3\text{Fe}_5\text{O}_{12}$ and $\text{SrFe}_{12}\text{O}_{19}$ magneto-optic crystals.^(22–25)

In the present study, we demonstrated the high-speed epitaxial growth of a $\text{Eu}^{3+}:\text{Y}_2\text{O}_3$ thick film phosphor. The epitaxial growth mode, microstructure, and photo- and radioluminescence properties of the film were examined.

2. Materials and Methods

The laser-assisted metal–organic CVD apparatus has been described elsewhere.⁽²⁶⁾ The metal–organic compounds of yttrium tris (dipivaloylmethanate) (Kojundo Chemical Lab. Co. Ltd., Japan) and europium tetrakis(dipivaloylmethanate) (Toshima Manufacturing Co., Ltd., Japan) were maintained at temperatures of 463 and 473 K, respectively, in precursor furnaces. The resultant vapor was transferred to the CVD chamber using Ar (purity: 99.9999%) as the carrier gas, and O_2 gas (99.5%) was separately introduced to the chamber through a double-tubed nozzle. The molar ratio in the precursor vapor was estimated from the mass change in each precursor before and after deposition, and it was calculated to be $\text{Eu}:\text{Y} = 3:97$ [$(\text{Eu}_{0.03}\text{Y}_{0.97})_2\text{O}_3$]. The total chamber pressure was maintained at 0.2 kPa.

The substrate was a (100) yttria-stabilized zirconia single-crystal plate (YSZ; $5 \times 5 \times 0.5 \text{ mm}^3$) polished on both sides. The substrate was preheated to 1000 K on a heating stage, then irradiated with a CO_2 laser (wavelength: 10.6 μm ; maximum laser output: 60 W; SPT Laser Technology Co., Ltd., China) through a ZnSe window. The substrate was heated to 1323 K using laser irradiation. The target thickness was 7 μm on the basis of the mean free path of 8 keV X-rays for Y_2O_3 , and thus the deposition time was set to 0.6 ks.

The phase composition and out-of-plane orientation of the resultant film were identified by X-ray diffraction (XRD; Bruker D2 Phaser, USA), and the in-plane orientation was studied by X-ray pole figure measurement (Rigaku Ultima IV, Japan). The crystal structures were visualized using the VESTA software package.⁽²⁷⁾ The microstructure was observed using a scanning electron microscope (SEM; JEOL JCM-6000, Japan). The in-line transmittance was measured using a UV–visible spectrophotometer (JASCO V-630, Japan) in the 190–1100 nm wavelength range. The photoluminescence (PL) and PL excitation (PLE) spectra and the decay profile were measured using a fluorescence spectrophotometer (JASCO FP-8300, Japan).

The X-ray-excited luminescence (XEL) spectrum was measured using a spectrometer (Ocean Insights HR2000+, USA) under continuous X-ray irradiation generated from an X-ray tube (Cu target) operated at 40 kV and 40 mA without any monochromators or filters. For comparison, a commercially available $\text{Bi}_4\text{Ge}_3\text{O}_{12}$ (BGO) single crystal ($5 \times 5 \times 1 \text{ mm}^3$; light yield: 8500 ph MeV^{-1} ; Epic Crystal Co., Ltd., China) was evaluated in the same setup.⁽²⁸⁾

3. Results and Discussion

Figures 1(a) and 1(b) respectively show out-of-plane and in-plane XRD patterns of the resultant film. The $\text{Eu}^{3+}:\text{Y}_2\text{O}_3$ thick film was indexed as a cubic bixbyite structure (ICSD No. 23811; $Ia\bar{3}d$ and $a = 1.064$ nm) with (100) orientation [Fig. 1(a)]. X-ray pole measurements of the $\{111\}$ plane of both the $\text{Eu}^{3+}:\text{Y}_2\text{O}_3$ thick film and the YSZ substrate confirmed that the (100) $\text{Eu}^{3+}:\text{Y}_2\text{O}_3$ thick film grew epitaxially on the (100) YSZ substrate with the in-plane orientation relationship of $[001] \text{Eu}^{3+}:\text{Y}_2\text{O}_3 \parallel [001] \text{YSZ}$ [Fig. 1(b)]. Since the lattice mismatch between the Y_2O_3 and YSZ cubic structures is small (3.3%), the (100) $\text{Eu}^{3+}:\text{Y}_2\text{O}_3$ thick film epitaxially grew on the (100) YSZ substrate with a cube-on-cube growth mode, as shown in Fig. 1(d).

Figure 2(a) shows cross-sectional and surface SEM images of the $\text{Eu}^{3+}:\text{Y}_2\text{O}_3$ thick film grown on the YSZ substrate. The $\text{Eu}^{3+}:\text{Y}_2\text{O}_3$ film exhibited a 7- μm -thick dense cross section with a

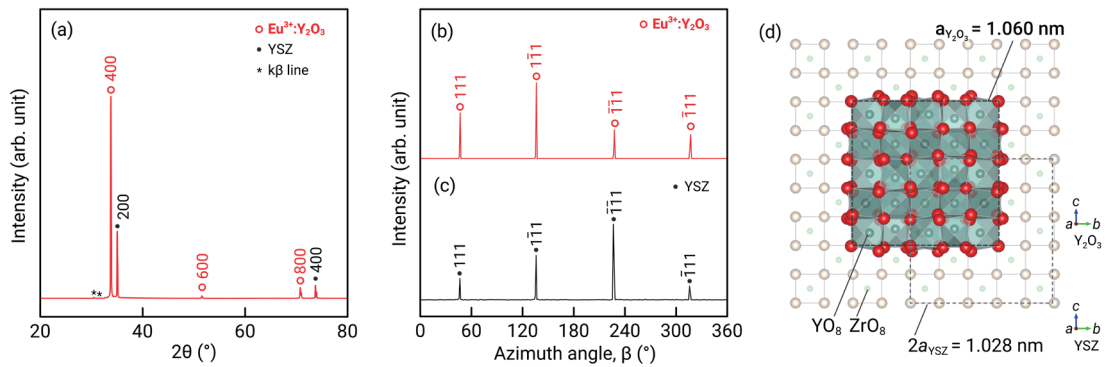


Fig. 1. (Color online) (a) Out-of-plane XRD pattern of the $\text{Eu}^{3+}:\text{Y}_2\text{O}_3$ thick film prepared on a (100) YSZ substrate, and in-plane XRD patterns of (b) Y_2O_3 $\{111\}$ plane and (c) YSZ $\{111\}$ plane. (d) Schematic plan view of the epitaxial relationship between the (100) $\text{Eu}^{3+}:\text{Y}_2\text{O}_3$ thick film and the (100) YSZ substrate.

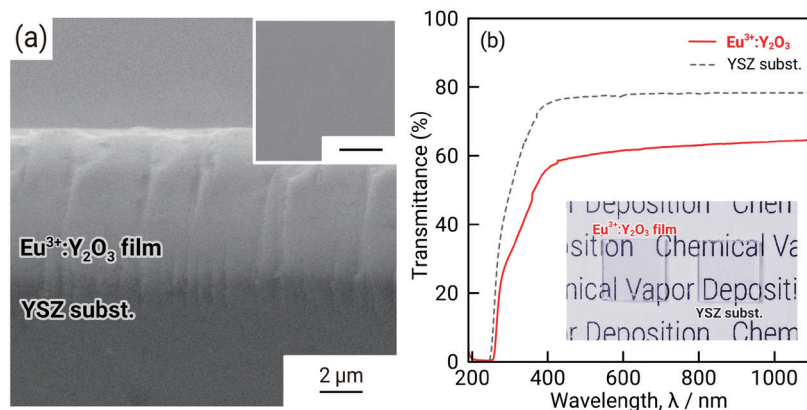


Fig. 2. (Color online) (a) Cross-sectional SEM image of the (100) $\text{Eu}^{3+}:\text{Y}_2\text{O}_3$ thick film epitaxially grown on the YSZ substrate. The inset shows a surface SEM image with a scale bar of 2 μm . (b) In-line transmittance spectra of the (100) $\text{Eu}^{3+}:\text{Y}_2\text{O}_3$ thick film on the YSZ substrate (solid line) and the raw YSZ substrate (dashed line). The inset shows a photograph of the $\text{Eu}^{3+}:\text{Y}_2\text{O}_3$ thick film on the YSZ substrate and the raw YSZ substrate.

smooth surface. From the cross-sectional SEM image and deposition time, the deposition rate was calculated to be $42 \mu\text{m h}^{-1}$, which was 840–10500 times higher than those of $\text{Eu}^{3+}:\text{Y}_2\text{O}_3$ thin films prepared using the sol–gel ($0.05 \mu\text{m h}^{-1}$), CVD ($0.004 \mu\text{m h}^{-1}$), and chemical bath deposition ($0.004 \mu\text{m h}^{-1}$) methods.^(15–17) Figure 2(b) shows the in-line transmittance spectra of the $\text{Eu}^{3+}:\text{Y}_2\text{O}_3$ thick film on the YSZ substrate and the raw YSZ substrate. The in-line transmittance of the $\text{Eu}^{3+}:\text{Y}_2\text{O}_3$ thick film at a wavelength of 600 nm was 81% of that of the raw YSZ substrate.

Figure 3 shows PLE and PL spectra and the PL decay profile of the $\text{Eu}^{3+}:\text{Y}_2\text{O}_3$ thick film prepared on the YSZ substrate. In the PLE spectrum of the $\text{Eu}^{3+}:\text{Y}_2\text{O}_3$ thick film monitored at an emission wavelength of 612 nm, the sharp peaks in the wavelength range of 300–500 nm were associated with 4f–4f transitions due to Eu^{3+} ions and the broad band centered at 240 nm was derived from the $\text{O}^{2-}-\text{Eu}^{3+}$ charge transfer band (CTB). The PL spectrum is composed of ${}^5\text{D}_{0,1,2}\rightarrow{}^7\text{F}_J$ ($J = 0-4$) transitions of the Eu^{3+} ions [Fig. 3(a)]. The probability of the ${}^5\text{D}_0\rightarrow{}^7\text{F}_2$ electric-dipole transition at 612 nm is sensitive to the symmetry of the surrounding Eu^{3+} , while the ${}^5\text{D}_0\rightarrow{}^7\text{F}_1$ magnetic-dipole transition at 593 nm is independent of the surrounding symmetry. Therefore, a large asymmetry ratio, i.e., a large intensity ratio of ${}^5\text{D}_0\rightarrow{}^7\text{F}_2$ to ${}^5\text{D}_0\rightarrow{}^7\text{F}_1$ emissions, implies a low symmetry of the surrounding Eu^{3+} ions.⁽²⁹⁾ In the Y_2O_3 bixbyite structure, Y^{3+} and Eu^{3+} are located at either a non-centrosymmetric C_2 site or a centrosymmetric S_6 (C_{3i}) site.⁽³⁰⁾ The Y_2O_3 bixbyite structure has three times more C_2 sites than S_6 sites, resulting in an intense emission associated with the ${}^5\text{D}_0\rightarrow{}^7\text{F}_2$ transition, as observed in the PL spectrum. The asymmetry ratio of the $\text{Eu}^{3+}:\text{Y}_2\text{O}_3$ thick film was estimated as 6.2, which is comparable to the reported values for $\text{Eu}^{3+}:\text{Y}_2\text{O}_3$ nanocrystals (5.1–6.7).^(31,32) The PL decay profile of the $\text{Eu}^{3+}:\text{Y}_2\text{O}_3$ thick film measured at 612 nm for the ${}^5\text{D}_0\rightarrow{}^7\text{F}_2$ transition under the CTB excitation at 240 nm indicated a single exponential time constant. The decay time constant was calculated as 1.7 ms [Fig. 3(b)], which is comparable to those reported in the literature (1.0–2.0 ms).^(33–35)

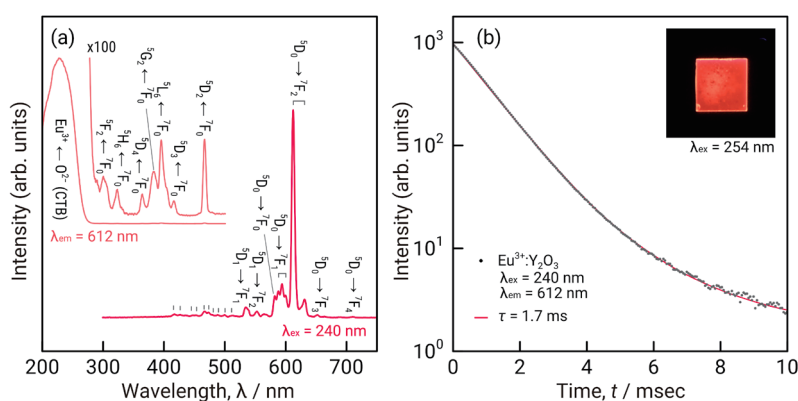


Fig. 3. (Color online) (a) PLE spectrum monitored at 612 nm and PL spectrum excited at 240 nm, and (b) PL decay profile monitored at 612 nm and excited at 240 nm of the $\text{Eu}^{3+}:\text{Y}_2\text{O}_3$ thick film grown on the YSZ substrate. Vertical ticks in the PL spectrum indicate possible transitions from high-energy excitation states of ${}^5\text{D}_2$ and ${}^5\text{D}_3$ to ${}^7\text{F}_J$ states.^(36,37) The inset in the PL decay profile shows a photograph of the $\text{Eu}^{3+}:\text{Y}_2\text{O}_3$ thick film on the YSZ substrate under irradiation by UV light ($\lambda = 254 \text{ nm}$) from a low-pressure mercury-vapor lamp.

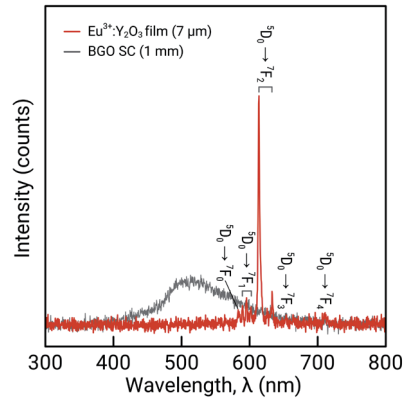


Fig. 4. (Color online) X-ray-induced radioluminescence spectra of the $\text{Eu}^{3+}:\text{Y}_2\text{O}_3$ thick film grown on the YSZ substrate and a BGO single crystal measured with the X-ray tube operating at 40 kV and 40 mA.

Figure 4 shows the radioluminescence spectra of the 7- μm -thick $\text{Eu}^{3+}:\text{Y}_2\text{O}_3$ thick film grown on the YSZ substrate and a 1-mm-thick BGO single crystal under X-ray irradiation. The $\text{Eu}^{3+}:\text{Y}_2\text{O}_3$ thick film exhibited a sharp emission at 612 nm from the $^5\text{D}_0 \rightarrow ^7\text{F}_2$ transition of Eu^{3+} ions, while the BGO single crystal showed a broad emission at 350–700 nm. The integrated luminescence intensity of the $\text{Eu}^{3+}:\text{Y}_2\text{O}_3$ thick film over the range of 500–700 nm was 15% of that of the BGO single crystal over the range of 350–700 nm.

The difference in the observed integrated luminescence intensity between the BGO reference crystal and the $\text{Eu}^{3+}:\text{Y}_2\text{O}_3$ thick film is associated with the combination of the X-ray attenuation length of each material and the spectrum of the irradiated X-ray energy. The X-ray attenuation length was calculated using the attenuation coefficients obtained from Henke's table.⁽¹⁸⁾ The attenuation coefficients for BGO at 40 keV, Y_2O_3 at 40 keV, and Y_2O_3 at 8 keV are 74, 41, and 1782 cm^{-1} , respectively. The following equation is used to calculate the absorbance rate from the attenuation coefficient:

$$I = I_0 e^{-\mu x}, \quad (1)$$

$$A = 1 - e^{-\mu x}, \quad (2)$$

where I is the intensity of the transmitted X-rays, I_0 is the intensity of the incident X-rays, μ is the attenuation coefficient, x is the thickness of the scintillator, and A is absorbance rate. The mean free path was calculated as the material thickness that can reduce the X-ray intensity to a factor of $1/e$.

We used a non-monochromatized X-ray source for radioluminescence spectroscopy, and thus the 1-mm-thick BGO reference crystal absorbed almost the entire X-ray photon energy up to 40 keV in the irradiated X-rays. Although 97% of high-energy X-ray photons passed through the 7- μm -thick $\text{Eu}^{3+}:\text{Y}_2\text{O}_3$ in the present radioluminescence measurement, a low-energy monochromatized X-ray source has often been applied for high-resolution radiation imaging. For example, 8 keV X-ray photons associated with $\text{Cu K}\alpha$ radiation can be sufficiently blocked by an

Y₂O₃ thick film phosphor with 7–13 μm thickness. Therefore, the resultant 7-μm-thick Eu³⁺:Y₂O₃ is a candidate scintillation screen for microtomography techniques. The correlation between the film thickness and light yield in X-ray imaging tests will be studied in future work.

4. Conclusions

We prepared a Eu³⁺:Y₂O₃ thick film phosphor on a (100) YSZ substrate by laser-assisted metal–organic CVD. The (100) Eu³⁺:Y₂O₃ film was epitaxially grown on a (100) YSZ substrate with the cube-on-cube growth mode, and the deposition rate reached 42 μm h⁻¹. The in-line transmittance at 600 nm of the Eu³⁺:Y₂O₃ thick film reached 81% of that of the YSZ substrate. Under UV and X-ray irradiation, the Eu³⁺:Y₂O₃ thick film emitted red emission light at 612 nm, originating from the ⁵D₀→⁷F₂ transition of the Eu³⁺ centers. Laser-assisted metal–organic CVD can be a rapid production process for Y₂O₃-based thick film phosphors potentially used in X-ray imaging systems.

Acknowledgments

This study was supported in part by JSPS KAKENHI Grant Numbers JP17H03426, JP20H02477, JP20H05186, 21J11881, and 21H05199. This study was also supported in part by YNU-GSEIS Joint Research Project B and Yokohama Kogokai. The X-ray pole measurement (Ultima IV) was carried out at the Instrumental Analysis Center, Yokohama National University.

References

- 1 C. W. E. van Eijk: *Phys. Med. Biol.* **47** (2002) R85. <https://doi.org/10.1088/0031-9155/47/8/201>
- 2 T. Yanagida: *Opt. Mater.* **35** (2013) 1987. <https://doi.org/10.1016/j.optmat.2012.11.002>
- 3 T. Yanagida: *Proc. Jpn. Acad. Ser. B* **94** (2018) 75–97. <https://doi.org/10.2183/pjab.94.007>
- 4 D. R. Schaart, H. T. van Dam, S. Seifert, R. Vinke, P. Dendooven, H. Löhner, and F. J. Beekman: *Phys. Med. Biol.* **54** (2009) 3501. <https://doi.org/10.1088/0031-9155/54/11/015>
- 5 J. Glodo, Y. Wang, R. Shawgo, C. Brecher, R. H. Hawrami, J. Tower, and K. S. Shah: *Phys. Procedia* **90** (2017) 285. <https://doi.org/10.1016/j.phpro.2017.09.012>
- 6 S. Yamamoto and H. Tomita: *Radiat. Meas.* **115** (2018) 13. <https://doi.org/10.1016/j.radmeas.2018.05.009>
- 7 T. Yanagida, Y. Fujimoto, A. Yamaji, N. Kawaguchi, K. Kamada, D. Totsuka, K. Fukuda, K. Yamanoi, R. Nishi, S. Kurosawa, T. Shimizu, and N. Sarukura: *Radiat. Meas.* **55** (2013) 99. <https://doi.org/10.1016/j.radmeas.2012.05.014>
- 8 B. K. Cha, J.-H. Shin, J. Y. Kim, H. Jeon, J. H. Bae, C.-H. Lee, S. Chang, H. Kim, B.-J. Kim, and G. Cho: 2008 IEEE Nuclear Science Symp. Conference Record (2008). <https://doi.org/10.1109/NSSMIC.2008.4774627>
- 9 H. Kato, T. Fujiwara, B. E. O'Rourke, H. Toyokawa, A. Koike, T. Aoki, and R. Suzuki: *Sens. Mater.* **28** (2016) 763. <https://doi.org/10.18494/SAM.2016.1249>
- 10 K. Tabata, R. Ohtake, and T. Aoki: *Sens. Mater.* **32** (2020) 4037. <https://doi.org/10.18494/SAM.2020.2963>
- 11 T. Martin and A. Koch: *J. Synchrotron Radiat.* **13** (2006) 180. <https://doi.org/10.1107/S0909049506000550>
- 12 T. Tomiki, J. Tamashiro, Y. Tanahara, A. Yamada, H. Fukutani, T. Miyahara, H. Kato, S. Shin, and M. Ishigame: *J. Phys. Soc. Jpn.* **55** (1986) 4543. <https://doi.org/10.1143/JPSJ.55.4543>
- 13 G. Blasse: *Chem. Mater.* **6** (1994) 1465. <https://doi.org/10.1021/cm00045a002>
- 14 D. Djurovic, M. Zinkevich, and F. Aldinger: *Calphad* **31** (2007) 560. <https://doi.org/10.1016/j.calphad.2007.01.010>
- 15 S. Y. Jung and K. J. Kim: *J. Ceram. Soc. Jpn.* **119** (2011) 616. <https://doi.org/10.2109/jcersj2.119.616>
- 16 J. Wang, Z. Zhang, X. Guo, J. Zhao, H. Chen, and X. Yang: *J. Rare Earths* **28** (2010) 684. [https://doi.org/10.1016/S1002-0721\(09\)60179-4](https://doi.org/10.1016/S1002-0721(09)60179-4)

- 17 N. Harada, A. Ferrier, D. Serrano, M. Persechino, E. Briand, R. Bachelet, I. Vickridge, J.-J. Ganem, P. Goldner, and A. Tallaire: *J. Appl. Phys.* **128** (2020) 055304. <https://doi.org/10.1063/5.0010833>
- 18 B. L. Henke, E. M. Gullikson, and J. C. Davis: *At. Data Nucl. Data Tables* **54** (1993) 181. <https://doi.org/10.1006/adnd.1993.1013>
- 19 S. Matsumoto, Y. Kaneda, and A. Ito: *Ceram. Int.* **46** (2020) 1810. <https://doi.org/10.1016/j.ceramint.2019.09.156>
- 20 A. Ito and Y. Morishita: *Mater. Lett.* **258** (2020) 126817. <https://doi.org/10.1016/j.matlet.2019.126817>
- 21 S. Matsumoto and A. Ito: *J. Ceram. Soc. Jpn.* **129** (2021) 1. <https://doi.org/10.2109/jcersj2.20156>
- 22 S. Matsumoto and A. Ito: *Opt. Mater. Express* **10** (2020) 899. <https://doi.org/10.1364/OME.386425>
- 23 P. Zhao, A. Ito, and T. Goto: *Surf. Coat. Technol.* **235** (2013) 273. <https://doi.org/10.1016/j.surfcoat.2013.07.048>
- 24 H. Aida, R. Watanuki, and A. Ito: *Mater. Lett.* **276** (2020) 128228. <https://doi.org/10.1016/j.matlet.2020.128228>
- 25 K. Kato, R. Watanuki, and A. Ito: *Mater. Lett.* **274** (2020) 128046. <https://doi.org/10.1016/j.matlet.2020.128046>
- 26 A. Ito, H. Kadokura, T. Kimura, and T. Goto: *J. Alloys Compd.* **489** (2010) 469. <https://doi.org/10.1016/j.jallcom.2009.09.088>
- 27 K. Momma and F. Izumi: *J. Appl. Crystallogr.* **44** (2011) 1272. <https://doi.org/10.1107/S0021889811038970>
- 28 BGO crystal - BGO scintillator crystal: <https://www.epic-crystal.com/oxide-scintillators/bgo-scintillator.html> (accessed October 2021).
- 29 K. Binnemans: *Coord. Chem. Rev.* **295** (2015) 1. <https://doi.org/10.1016/j.ccr.2015.02.015>
- 30 F. Hanic, M. Hartmanová, G. G. Knab, A. A. Urusovskaya, and K. S. Bagdasarov: *Acta Crystallogr. B* **40** (1984) 76. <https://doi.org/10.1107/S0108768184001774>
- 31 Z. Wei-Wei, Y. Min, H. Xing-Dao, and G. Yi-Qing: *J. Alloys Compd.* **509** (2011) 3613. <https://doi.org/10.1016/j.jallcom.2010.12.110>
- 32 R. H. Krishna, B. M. Nagabhushana, H. Nagabhushana, N. S. Murthy, S. C. Sharma, C. Shivakumara, and R. P. S. Chakradhar: *J. Phys. Chem. C* **117** (2013) 1915. <https://doi.org/10.1021/jp309684b>
- 33 A. Gupta, N. Brahme, and D. P. Bisen: *Phys. Procedia* **76** (2015) 16. <https://doi.org/10.1016/j.phpro.2015.10.004>
- 34 J. Kaszewski, J. Rosowska, B. S. Witkowski, Ł. Wachnicki, K. Wenelska, E. Mijowska, L.-I. Bulyk, D. Włodarczyk, A. Suchocki, B. Kozankiewicz, and M. Godlewski: *J. Rare Earths* **37** (2019) 1206. <https://doi.org/10.1016/j.jre.2019.04.011>
- 35 W.-W. Zhang, W.-P. Zhang, P.-B. Xie, M. Yin, H.-T. Chen, L. Jing, Y.-S. Zhang, L.-R. Lou, and S.-D. Xia: *J. Colloid Interface Sci.* **262** (2003) 588. [https://doi.org/10.1016/S0021-9797\(03\)00169-3](https://doi.org/10.1016/S0021-9797(03)00169-3)
- 36 R. G. Pappalardo and R. B. Hunt: *J. Electrochem. Soc.* **132** (1985) 721. <https://doi.org/10.1149/1.2113940>
- 37 G. A. Hirata, J. McKittrick, M. Avalos-Borja, J. M. Siqueiros, and D. Devlin: *Appl. Surf. Sci.* **113–114** (1997) 509. [https://doi.org/10.1016/S0169-4332\(96\)00829-X](https://doi.org/10.1016/S0169-4332(96)00829-X)